HOMODYNE DETECTION OF MULTIMODE OPTICAL SIGNALS

A THESIS

SUBMITTED TO THE DEPARTMENT OF ELECTRICAL AND ELECTRONICS ENGINEERING

AND THE INSTITUTE OF ENGINEERING AND SCIENCES

OF BILKENT UNIVERSITY

IN PARTIAL FULFILLMENT OF THE REQUIREMENTS

FOR THE DEGREE OF

MASTER OF SCIENCE

By

Mujtaba Fidaul Haq

July, 1991

HOMODYNE DETECTION OF MULTIMODE OPTICAL SIGNALS

A THESIS
SUBMITTED TO THE DEPARTMENT OF ELECTRICAL & ELECTRONICS
ENGINEERING
AND THE INSTITUTE OF ENGINEERING AND SCIENCES
OF BILKENT UNIVERSITY
IN PARTIAL FULFILLMENT OF THE REQUIREMENTS
FOR THE DEGREE OF
MASTER OF SCIENCE

By
Mujtaba Fidaul Haq
1991

Mujtaba Fidaul Haq

tarafından [illegible]

I certify that I have read this thesis and that in my opinion it is fully adequate, in scope and in quality, as a thesis for the degree of Master of Science.

Assist. Prof. GürhanŞaplakoğlu (Principal Advisor)

I certify that I have read this thesis and that in my opinion it is fully adequate, in scope and in quality, as a thesis for the degree of Master of Science.

Assoc. Prof. Ayhan Altıntaş

I certify that I have read this thesis and that in my opinion it is fully adequate, in scope and in quality, as a thesis for the degree of Master of Science.

Prof. Dr. Hayrettin Köymen

Approved for the Institute of Engineering and Sciences:

Prof. Dr. Mehmet Baray
Director of Institute of Engineering and Sciences

ABSTRACT

HOMODYNE DETECTION OF MULTIMODE OPTICAL SIGNALS

Mujtaba Fidaul Haq
M.S. in Electrical & Electronics Engineering
Supervisor: Assist. Prof. GürhanŞaplakoğlu
July 1991

The feasibility of coherent homodyne detection for multimode optical sources is experimentally investigated. By employing the self-homodyne detection, it is observed that a considerable amount of mixing can take place between the signal and local oscillator fields despite the relatively small coherence length of multimode lasers. The experiment was carried out using an all-atmospheric set-up, necessitating a thorough calculation of power losses due to beam misalignment. Power losses in the interference term for radial and angular misalignments were calculated for first order Gaussian beams. It is seen that radial misalignment is intolerable for beam radii ratios smaller than 0.35 whereas angular misalignment becomes intolerable for angular deviations greater than a few tens of milli degrees.

Key words : Coherent detection, Optical communication, Gaussian beam misalignment.

ÖZET

ÇOK MODLU OPTİK SİNYALLERİN HOMODİN ALGILAMASI

Mujtaba Fidaul Haq
Elektrik ve Elektronik Mühendisliği Bölümü Yüksek Lisans
Tez Yöneticisi: Assist. Prof. GürhanŞaplakoğlu
July 1991

Eşevre homodin haberleşmede çok modlu optik kaynakların uygunluğu deneysel olarak incelendi. Çalışmada self-homodinleme denen bir teknik kullanarak göründü ki, çok modlu lazer kaynaklarının eşevre mesafesinin tek modlu kaynaklarınınkine göre nispeten kısa olmasına rağmen sinyal ve yerel osilatör arasında büyük derecede homodin girişim yer almaktadır. Deney tüm atmosferik bir düzenlemeyle yapıldığı için demetlerin uyuşmazlığından dolayı ortaya çıkan güç kayıpları teorik olarak hesaplandı. Girişim terimindeki bu güç kayıpları birbirinden ayrılmış bir şeklinde radyal ve açısal uyuşmazlıklar için ayrı ayrı grafikler halinde sunuldu. Radyal kayıpların demet yarıçapları arasındaki uyuşmazlık 0.35 civarında olana kadar, açısal kayıpların ise 1 miliradyanın ondabiri seviyesine kadar önemli olmadığı hesaplanmıştır.

Anahtar kelimeler : Eşevre algılama, Optik haberleşme, Gaus demetlerin uyuşmazlığı.

ACKNOWLEDGMENT

I would like to express my most grateful thanks to my supervisor Assistant Professor Gürhan Şaplakoğlu who has guided and encouraged me during the development of this thesis.

I would also like to express my gratitude to Professor Abdullah Atalar and Associate Professor Ayhan Altıntaş, who provided me with most useful advices and comments from time to time.

I also heartily appreciate my colleague Ogan Ocalı for his valuable discussions.

Contents

List of Figures

Chapter 1

Introduction

Optical homodyne detection is a subclass of coherent optical detection schemes and hence, like all coherent detection schemes, includes a local oscillator at the receiver front-end. In coherent detection, the received optical signal field is mixed with a coherent optical local oscillator field before falling onto the photodetector surface[1]. Although photodetectors are square-law devices and hence capable of sensing intensity variations only, coherent detection schemes detect complex field amplitudes, i.e. field magnitude and phase as a result of this mixing[2]. In the case of homodyne detection, the local oscillator field must be exactly in phase and have the same frequency as the carrier field of the incoming modulated signal[3]. A simplified block diagram of basic homodyne receiver is shown in figure 1.1.

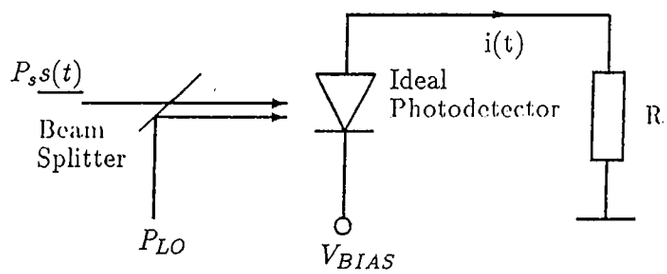

Figure 1.1: Simplified block diagram of a homodyne receiver

The signal field incident onto the ideal noiseless photodetector surface is represented by $\sqrt{P_s}\underline{s}(t)$ where P_s is the average signal power and $\underline{s}(t)$ is the normalized[1] complex envelope of the modulating signal. A more rigorous notation would warrant that we express the signal field as $\vec{E}_s\, e^{j(w_s t - kz - \phi_s)}\underline{s}(t)$, in which case the vector field amplitude $\vec{E}_s$ indicates the direction of polarization of the field and $P_s = \frac{1}{2}\vec{E}_s \bullet \vec{E}_s^{\star}$ is the power of the field[1]. Moreover, it is assumed that the field propagates in the positive z direction with an angular frequency of w_s and an initial phase of ϕ_s. The assumption that the signal field oscillates at a single frequency makes it a single mode field. Keeping with the same vain, the single mode local oscillator field $\sqrt{P_{LO}}$ should also be expressed as $\vec{E}_{LO}\, e^{j(w_{LO}t - kz - \phi_{LO})}$. But for efficient mixing on the photodetector surface, the signal and local oscillator fields must have the same direction of polarization and are incident onto the photodetector surface along the same axis of propagation. Consequently, the fields can be represented as scalar functions without loss of generality, with an underlying assumption of perfect polarization matching. Furthermore, the local oscillator field has exactly the same frequency as and is completely in phase with the signal field. So, if we let the photodetector surface to be located at $z = 0$, it becomes apparent that the signal field can be correctly abbreviated as $\sqrt{P_s}\underline{s}(t)$ and the local oscillator field as $\sqrt{P_{LO}}$. The name "coherent detection" is indicative of this strict relationship between the signal and local oscillator fields. When these two fields are made to fall onto the surface of an ideal photodetector by means of a beam splitter, the photodetector produces a current whose mean value is proportional to the magnitude square of the combined incident field,

$$\begin{aligned} \overline{i(t)} &= K\|\sqrt{P_{LO}} + \sqrt{P_s}\underline{s}(t)\|^2 \\ &= K\left[P_{LO} + P_s\|\underline{s}(t)\|^2 + 2\sqrt{(P_{LO}P_s)}Re\{\underline{s}(t)\}\right] \end{aligned} \tag{1.1}$$

where overbar denotes expectation and K is a constant that depends on the responsivity[2] of the detector. In detection receivers, the local oscillator power P_{LO} is much higher

[1] $\frac{1}{T_s}\int_0^{T_s}\|\underline{s}(t)\|^2 dt = 1$ for some signaling time interval $(0, T_s)$.

[2] Responsivity (A/W) of a detector is the measure of the efficiency by which the electro-optic conversion takes place.

than the signal power P_s. Consequently, equation 1.1 can be simplified as,

$$\overline{i(t)} \simeq K\left[P_{LO} + 2\sqrt{(P_{LO}P_s)}Re\{\underline{s}(t)\}\right] . \tag{1.2}$$

By employing a suitable filtering technique or a clever detection configuration, we can get rid of the unwanted dc term KP_{LO} which leaves us the desired signal term $2\sqrt{(P_{LO}P_s)}Re\{\underline{s}(t)\}$. Furthermore, since P_{LO} can be arbitrarily large the above signal term can be pushed to a level well above the thermal noise of the receiver. This improvement in the SNR is the essence of coherent detection.

However, this simple description of homodyne detection is chiefly applicable for single mode signal and local oscillator fields, i.e. fields which, as mentioned above, oscillate at a single frequency. They are not generally valid for multimode fields. Multimode fields, which oscillate at a series of narrowly separated frequencies, generally can not be treated in the same fashion as the single mode fields.

In this thesis work, which is mainly about the implementation of a homodyne receiver, it is shown that coherent homodyne detection is also feasible for multimode lasers as long as we abide by the constraints brought about by the relatively short coherence length of multimode lasers. A homodyne detection set-up using multimode lasers was constructed and operated in the laboratory. The signal beam in the set-up is ASK modulated at 6MHz and a double balanced detector configuration is used as the receiver.

The purpose of the thesis was to gain practical experience in homodyne detection and related practical problems. As there is an acute lack of relevant information in the literature about down-to-earth practical problems involving optical set-ups, such an exercise in implementing a coherent detection set-up was both necessary and useful. One of the major practical problems was the misalignment of the signal and local oscillator beams incident onto the photodetector surface. It is seen that severe mixing losses can occur due to minute misalignments of the beams. These mixing losses are thoroughly investigated for the case of Gausian fields - the radiation field pattern of most of the lasers. To the best of our knowledge, these misalignment calculations for Gaussian beams do not exist anywhere in literature and can be useful to anyone dealing with atmospheric coherent detection schemes.

The next chapter, i.e. Chapter 2, contains the bulk of the thesis work. It begins with a section that explains the importance of coherence of sources in homodyne detection schemes followed by a section that describes the theory of homodyne detection in brief. The next section of the same chapter describes the set-up constructed for self-homodyne detection in the laboratory followed by a section that explains the double detection configuration employed in the set-up in detail. The last section of Chapter 2 deals with the geometric alignment problems. Chapter 3 contains the results in brief while the q-parameter calculations for the set-up for Gaussian beams is carried out in Appendix 1.

Chapter 2

Self-Homodyne Detection For Multimode Lasers

2.1 Importance of Coherence of Sources in Homodyne Detection

In the Optics and Waves Laboratory, we constructed a set-up for the homodyne detection of ASK modulated multimode laser signals. As was discussed in chapter 1, homodyne detection, or any coherent detection for that matter, requires perfect matching - both spatially and temporally - between the signal and local oscillator fields. Any mismatch, be it a poor correlation between the phase differences of the two fields or non identical diffraction patterns of the fields incident onto the photodetector surface or diffraction patterns slightly offset or slanted from each other, results in heavy penalty in terms of percent homodyne efficiency obtained. Multimode lasers, from this point of view, are limited by their relatively short coherence lengths. A multimode laser, unlike a single mode laser, has a series of longitudinal modes of oscillation. The frequency difference $\Delta\nu$ between two adjacent mode of oscillations is determined by the free spectral range of the laser [4]

$$\Delta\nu = c/2d \tag{2.1}$$

where c is the speed of light and d is the laser cavity length. The He-Ne multimode laser employed in the experimental set-up has a cavity length of 1 meter. It radiates

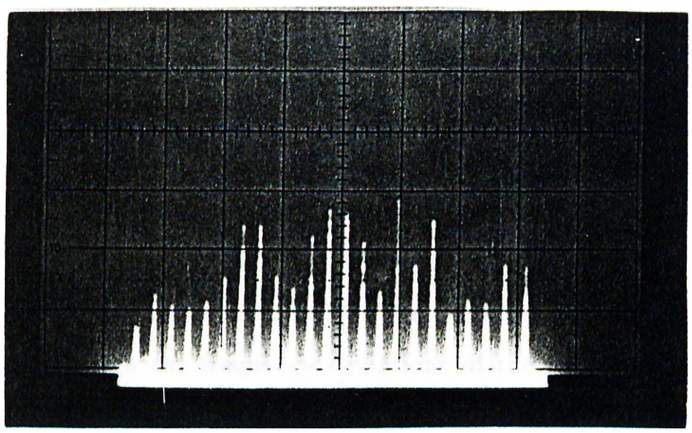

Figure 2.1: Frequency spectrum of the multimode laser

at the nominal wavelength of $\lambda = 632.8$nm and has got approximately twenty longitudinal modes of oscillation. A photograph of the frequency spectra of the laser is shown in figure 2.1. From equation 2.1 , the frequency difference between two adjacent modes is 150 MHz. The actual drawback of a multimode laser is the decrease in its actual coherence length by a factor inversely proportional to its total number of longitudinal modes. The coherence length of a nearly monochromatic source having a nominal wavelength of λ and spectral width $\Delta\nu$ can be expressed as[4]

$$l_c = c/2\Delta\nu \tag{2.2}$$

where c is again the speed of light. For approximately twenty longitudinal modes of oscillation, total spectral width of the He-Ne source used is 3GHz. This, in turn, implies that the coherence length of the multimode laser that we are using is approximately

$$\begin{aligned} l_{c_{MM}} &= \frac{3 \times 10^8 m/s}{2 \times 3GHz} \\ &= 5cm \end{aligned} \tag{2.3}$$

The import of this shortened coherence length will be appreciated in section 2.3 where the self-homodyne detection set-up constructed in the lab is explained in detail.

Now, we shall derive an expression to model the complex amplitude of the field radiated by a multimode laser. A single mode field can be represented as

$$\underline{\mathcal{U}}_{SM}(\overline{r},t) = \mathcal{U}_0 exp\big(j(\overline{k}\bullet\overline{r}+\phi+2\pi\nu_0 t)\big)\,, \tag{2.4}$$

where ν_0 is the center frequency of the single mode field. The longitudinal modes of a multimode laser can be thought of a series of single mode lasers though the two cases are not exactly equivalent[5]. The main reason for this discrepancy is the fact that although the frequency deviations of the individual modes are quite small and their bandwidths quite narrow compared to most of the commercially available diode lasers, the distribution of power among the individual modes is not fixed and in fact, stochastic in nature. But since the average power distribution among the modes is given by the overall gain curve of the laser and the fact that we perform the experiments within the shortened coherence length of the multimode laser as calculated above, we can approximate the multimode laser as an array of single mode lasers. This, in turn, permits us to write an equivalent mathematical representation for the mean complex field amplitude of a multimode laser having $2N+1$ longitudinal modes as

$$\underline{\mathcal{U}}_{MM}(\overline{r},t) = \sum_{n=-N}^{N} \mathcal{U}_{0n} exp\left(j((\overline{k}+\overline{\Delta k})\bullet\overline{r}+\phi_n+2\pi(\nu_0+n\Delta\nu)t)\right). \tag{2.5}$$

In this thesis, this representation of multimode fields will be used.

2.2 Brief Theory of Homodyne Detection

Now that we have modelled our multimode laser as a collection of a series of single mode lasers, we can go into a brief description of the theory behind homodyne detection. A block diagram of a basic homodyne receiver is shown in figure 2.2[1][3].

The signal field incident onto the ideal photodetector surface is represented by $\underline{\mathcal{U}}_s(\overline{r},t)$. Assuming that the detector is placed at the origin, i.e. at $z=0$ along the z-axis, the signal field on the detector surface can be written as

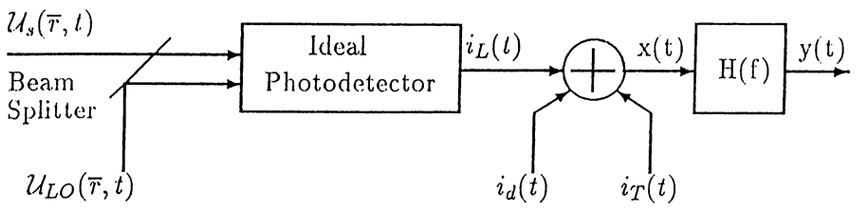

Figure 2.2: Block diagram of a homodyne receiver

$$\underline{\mathcal{U}}_s(\overline{r},t) = \left(\frac{4P_s}{\pi d^2}\right)^{\frac{1}{2}} \underline{s}(t) \tag{2.6}$$

where $\underline{s}(t)$ is a normalized complex envelope which satisfies $\frac{1}{T_s}\int_0^{T_s} \|\underline{s}(t)\|^2 dt = 1$ for some signaling time interval $(0, T_s)$. P_s is the time average signal field power and d is the diameter of the active photodetector surface. Similarly, on the detector surface, the local oscillator field $\underline{\mathcal{U}}_{LO}(\overline{r},t)$ can be expressed as

$$\underline{\mathcal{U}}_{LO}(\overline{r},t) = \left(\frac{4P_{LO}}{\pi d^2}\right)^{\frac{1}{2}} \tag{2.7}$$

where P_{LO} is the local oscillator field power. It should be noted that the local oscillator field has exactly the same frequency as and is completely in phase with the signal field. The photodetector current $i_L(t)$ is a Poisson process whose rate[1] is given by

$$\lambda(t) = \frac{\eta}{h\nu_0}\int d\overline{r}\, circ(2\|\overline{r}\|/d)\, \|\underline{\mathcal{U}}_s(\overline{r},t) + \underline{\mathcal{U}}_{LO}(\overline{r},t)\|^2 . \tag{2.8}$$

where

$$circ\left(\frac{2\|\overline{r}\|}{d}\right) = \begin{cases} 1 & \text{if } \|\overline{r}\| \le \frac{d}{2} \\ 0 & \text{if } \|\overline{r}\| \ge \frac{d}{2} \end{cases} \tag{2.9}$$

defines the active area of the photodetector. Moreover, η is the quantum efficiency of the photodetector and h is the Planck's constant. The expression for $\lambda(t)$ above, after some simplification can be written as

$$\lambda(t) = \frac{\eta}{h\nu_0}\left[P_{LO} + P_s\|\underline{s}(t)\|^2 + 2\sqrt{(P_{LO}P_s)}Re\{\underline{s}(t)\}\right] . \tag{2.10}$$

In addition to the shot noise inherent in the photodetector current $i_L(t)$, there are several additional noise sources present in the receiver front end. In particular,

$i_d(t)$ represents the dark current viz, the non zero current component present even in absence of LO and signal fields due to emission of thermally excited electrons and $i_T(t)$ which represents the thermal noise associated with the equivalent noise resistance of the front end electronics. Since the mean value of the thermal current $i_T(t)$ is zero, equation 2.10, from the theory of Poisson processes[1], implies that the mean value of the signal $x(t)$ [see figure 2.2] can be expressed as

$$\overline{x(t)} = q\lambda(t) + \overline{i_d(t)}\,, \tag{2.11}$$

where overbars denote expectation and q is the electron charge. Using equation 2.10, we can write equation 2.11 as

$$\overline{x(t)} = \mathcal{R}\left[P_{LO} + P_s\|\underline{s}(t)\|^2 + P_D + 2\sqrt{(P_{LO}P_s)}Re\{\underline{s}(t)\}\right]\,, \tag{2.12}$$

where $\mathcal{R} \equiv \frac{q\eta}{h\nu_0}$ is the responsivity of the photodetector and $\overline{i_d(t)}$ is replaced by its equivalent noise power term $\mathcal{R}P_D$. Again, using the theory of Poisson processes, it can be shown that the covariance of the signal $x(t)$ is[1]

$$\begin{aligned} K_{xx}(t,u) &= \left[q^2\lambda(t) + qI_D + 2kT/R\right]\delta(t-u) && (2.13)\\ &= \left[\frac{q^2\eta}{h\nu_0}(P_{LO} + P_s\|\underline{s}(t)\|^2 + 2\sqrt{(P_{LO}P_s)}Re\{\underline{s}(t)\}) + \right.\\ &\quad \left. qI_D + 2kT/R\right]\delta(t-u)\,. && (2.14)\end{aligned}$$

Here R is the receiver equivalent noise resistance, k is the Boltzmann's constant and T is the temperature of R in Kelvins and I_D is the average value of the dark current. The local oscillator power P_{LO} may be increased until $\frac{q^2\eta}{h\nu_0}P_{LO} \gg qI_D, 2kT/R$ and $\frac{q^2\eta}{h\nu_0}P_s$. In which case, equation 2.11 and 2.13 can be simplified as

$$\overline{x(t)} \simeq q\lambda(t)\,, \tag{2.15}$$

and

$$K_{xx}(t,u) = q^2\lambda(t)\delta(t-u)\,. \tag{2.16}$$

Physically, this is the essence of coherent detection : the mixing action with a strong local oscillator pushes the SNR well above the thermal and receiver noise levels, hence shot noise remains as the dominant noise source.

The covariance of the filtered signal $y(t)$ can be written as

$$K_{yy}(t,u) = \frac{q^2\eta}{h\nu_0} P_{LO} \int_{-\infty}^{\infty} d\tau h(t-\tau)h(u-\tau)\,. \tag{2.17}$$

Now if $h(t) = 1/2R\sqrt{P_{LO}}h'(t)$ where $h'(t)$ is a low pass filter with a bandwidth equal to W where W is much larger than the bandwidth of the modulating signal $\underline{s}(t)$ [see figure 2.3], then $K_{yy}(t,u)$ becomes

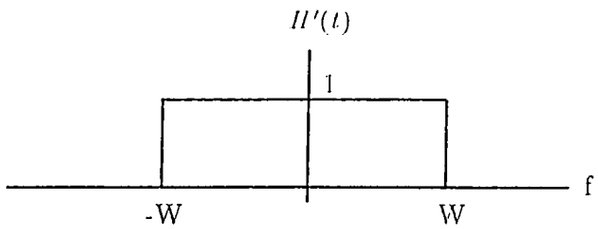

Figure 2.3: Low pass filter

$$K_{yy}(t,u) = \frac{h\nu_0}{4\eta} \int_{-\infty}^{\infty} d\tau h'(t-\tau)h'(u-\tau)\,. \tag{2.18}$$

With the above assumption of the local oscillator field and the low pass filter characteristic, the mean value of the filtered signal can be written as

$$\overline{y(t)} = \sqrt{P_s}Re\{\underline{s}(t)\} + \sqrt{P_{LO}}/2 \tag{2.19}$$

In effect, as mentioned previously, what is actually achieved in homodyne detection is the suppression of all other noise sources in the receiver by the presence of a strong local oscillator whose shot noise dominates the noise variance. So, we basically represent a homodyne detection scheme by the model shown in figure 2.4. Since in the limit when $\lambda \to \infty$ a Poisson process becomes a Gaussian process[6], a large local oscillator power means that $w(t)$ is a Gaussian process, and hence, it is completely characterized by its mean value $\overline{w}(t) = 0$ and autocorrelation function $\overline{w(t)w(u)} = \frac{h\nu_0}{4\eta}\delta(t-u)$. So, we can see that for a homodyne receiver, the signal-to-noise ratio is[1]

$$\begin{aligned} SNR_{hom} &= \frac{\frac{1}{T_s}\int_0^{T_s}(\overline{y}(t))^2\,dt}{Var(y(t))} \\ &= \frac{2\eta P_s}{h\nu_0 W}\,, \end{aligned} \tag{2.20}$$

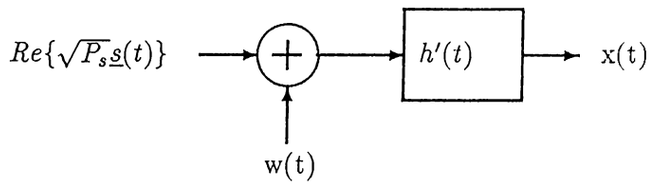

Figure 2.4: Model for homodyne detection

where $2W$ is the bandwidth of the receiver filter and $Var()$ denotes variance. This signal-to-noise ratio by far outperforms the signal-to-noise ratio of a direct detection receiver (in a direct detection receiver, the signal field is not mixed with a local oscillator field at the receiver front-end and is detected directly by the photodetector). The signal-to-noise ratio of a direct detection receiver is[2]

$$SNR_{DD} = \frac{\eta P_s}{2h\nu_0 W}. \tag{2.21}$$

which is only one fourth of the signal-to-noise ratio of a homodyne receiver.

2.3 Self-Homodyne Detection

In our homodyne detection set-up, instead of using a local oscillator laser source having the same phase and frequency as the incoming signal, a beam from the source laser was tapped and steered to be used as the local oscillator signal. This experimental technique is known as self-homodyne detection in literature[7]. The advantage of self-homodyning is that a phase and frequency locked local oscillator is derived from the signal itself reducing the complexity of the set-up. A block diagram of the homodyne detection set-up is shown in figure 2.5. The vertically polarized Gaussian beam coming out of the He-Ne laser is passed through the half-wave plate WP3 in order to change its plane of polarization so that the beam can be split by the polarizing beam splitter PBS1. The polarizing beam splitter lets the horizontally polarized component of the beam pass through while diverting the vertically polarized component of the beam at an angle of 90° with respect to the incoming beam. The ratio of the two beams can be adjusted by rotating the halfwave plate WP3. By a completely arbitrary choice, the horizontally polarized beam is used as the signal while the vertically polarized beam as the local oscillator. The

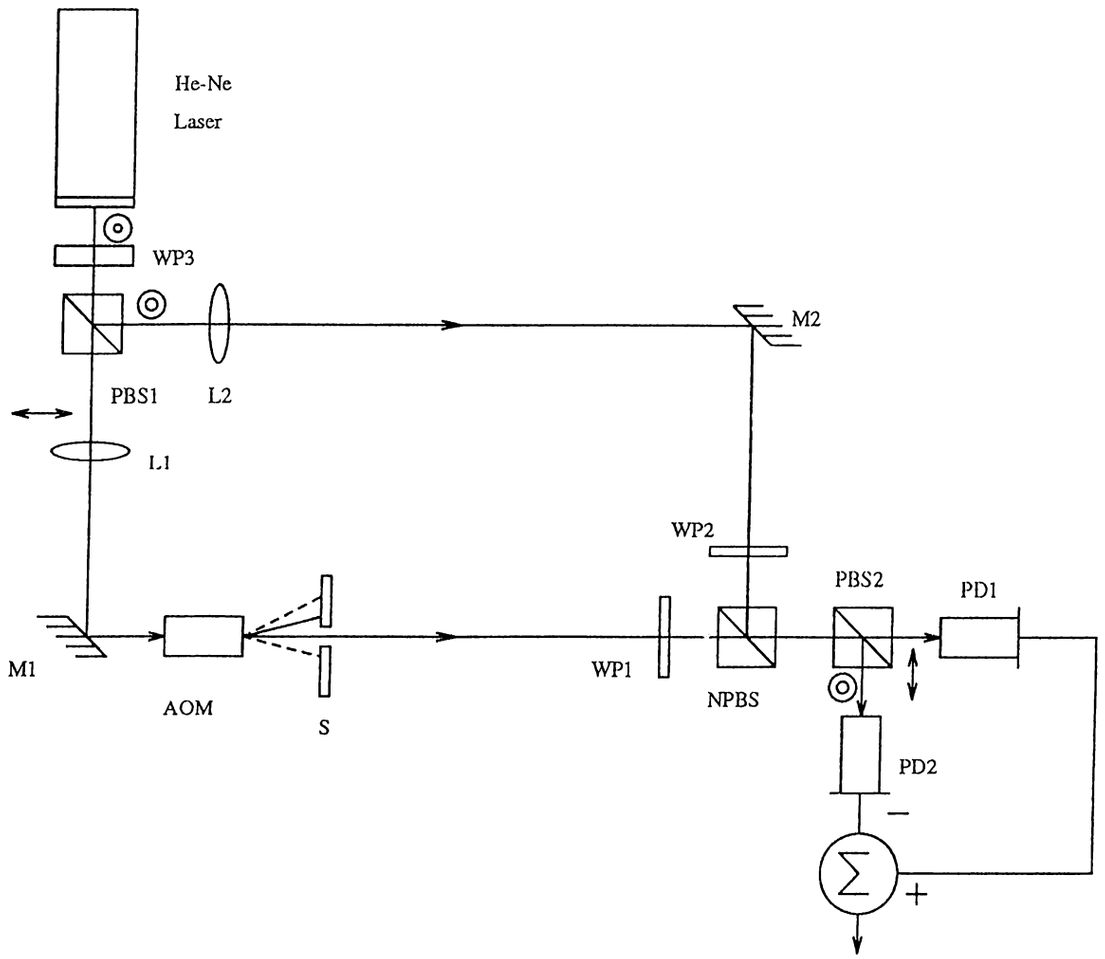

Figure 2.5: Block diagram of homodyne detection set-up

signal beam is then modulated by the acousto-optic modulator AOM. Lens L1 is used to focus the signal beam such that the beam radius is at its narrowest while passing through the Piezo-electric material inside the acousto-optic modulator. This is needed to drive the AOM at maximum possible bit rate. The narrower the beam radius of the signal passing through the AOM, the faster is its response[12]. The $\pm$1st order beams generated by the acousto-optic modulator is blocked by the slit S while only the zero order beam is allowed to pass to the receiver. Hence the signal is on-off modulated. The transmitter part of the set-up essentially consists of the components described so far. The sole purpose of the lens L2 placed on the local oscillator path is to match the beam radius and the radius of curvature of the LO field with those of the signal field. The importance of this mode matching and calculations of penalties

paid for lack of it is described in section 2.5 and exact calculations of beam waists and radii of curvatures of the Gaussian beams along the whole set-up is provided in Appendix A.

On the receiver side, the signal and local oscillator fields are mixed by the non polarizing beam splitter NBPS after passing through half-wave plates WP1 and WP2, respectively. WP1 and WP2 are used to change the polarization angles of the signal and local oscillator such that both the beams are now polarized at a plane making an angle of 45° with the horizontal plane. This ensures that the polarizing beam splitter PBS2 mixes the fields with a 50/50 ratio. The significance of this arrangement will become clear in the next subsection. At this point, it should also be mentioned that to guarantee coherent mixing of the LO and signal beams, the path difference between the beams should not exceed the coherence length of the multimode laser as found in equation 2.3. To be more precise, the difference between the paths the beams take between PBS1 and NPBS should not exceed 5cm.

Beams coming out of PBS2, which consists of both the local oscillator and signal beams, fall onto the photodetectors PD1 and PD2. The composite beam incident upon PD1 is horizontally polarized whereas the beam incident upon PD2, though equal in power, is vertically polarized. Finally, the photodetector currents generated by the incident optical fields are subtracted from one another which yields the desired detection current. This detector configuration employing two detectors and subtraction of detected currents from each other is known as double balanced detection and is explained in the next subsection.

2.4 Double Balanced Detection Configuration

The receiver section of the set-up in the laboratory employs a double balanced detector configuration. This type of detection provides a balanced detection of the two composite beams coming out of the last beam splitter. A detailed block diagram of the balanced receiver is shown in figure 2.6. The composite fields $\underline{\mathcal{U}}_{D1}$ and $\underline{\mathcal{U}}_{D2}$ are formed by mixing the signal and local oscillator fields and can be written as

$$\underline{\mathcal{U}}_{D1} = \sqrt{\epsilon}\,\underline{\mathcal{U}}_s + \sqrt{(1-\epsilon)}\,\underline{\mathcal{U}}_{LO}, \tag{2.22}$$

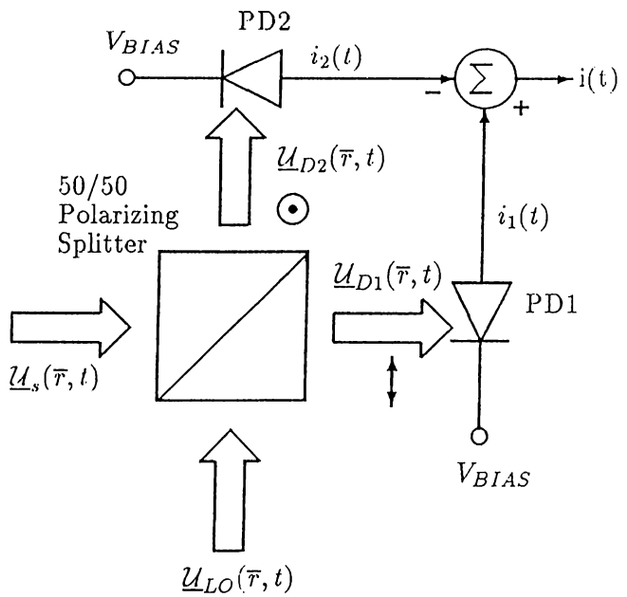

Figure 2.6: Double detection configuration

$$\underline{\mathcal{U}}_{D2} = -\sqrt{(1-\epsilon)}\,\underline{\mathcal{U}}_s + \sqrt{\epsilon}\,\underline{\mathcal{U}}_{LO}, \tag{2.23}$$

where ϵ is the intensity transmission coefficient and the negative sign in equation 2.23 is a consequence of the reciprocity theorem[9]. The corresponding intensities of the fields incident on the two detectors are,

$$\begin{aligned} p_1(t) &= \|\underline{\mathcal{U}}_{D1}\|^2 && (2.24)\\ &= \epsilon\|\underline{\mathcal{U}}_s\|^2 + (1-\epsilon)\|\underline{\mathcal{U}}_{LO}\|^2 + 2\sqrt{\epsilon(1-\epsilon)}\underline{\mathcal{U}}_{LO}\underline{\mathcal{U}}_s Re\{\underline{s}(t)\} && (2.25)\\ &\simeq (1-\epsilon)P_{LO} + 2\sqrt{\epsilon(1-\epsilon)}\sqrt{P_{LO}P_s}Re\{\underline{s}(t)\} && (2.26) \end{aligned}$$

for photodetector 1 and

$$\begin{aligned} p_2(t) &= \|\underline{\mathcal{U}}_{D2}\|^2 && (2.27)\\ &\simeq \epsilon P_{LO} - 2\sqrt{\epsilon(1-\epsilon)}\sqrt{P_{LO}P_s}Re\{\underline{s}(t)\} && (2.28) \end{aligned}$$

for photodetector 2. As usual, in equation 2.26 and 2.28, it is assumed that $P_{LO} = \|\underline{\mathcal{U}}_{LO}\|^2 \gg \|\underline{\mathcal{U}}_s\|^2 = P_s$. The mean values of the detector currents $i_1(t)$ and $i_2(t)$, as seen in chapter 1, are related to these power expressions. For the double detection configuration, taking $\epsilon = 1/2$ [since the signal and local oscillator fields

incident on the nonpolarizing beam splitter are polarized at an angle of 45°], the mean detector currents are

$$\overline{i_1(t)} = \mathcal{R}(P_{LO}/2 + \sqrt{P_{LO}P_S}Re\{\underline{s}(t)\}), \tag{2.29}$$

$$\overline{i_2(t)} = \mathcal{R}(P_{LO}/2 - \sqrt{P_{LO}P_S}Re\{\underline{s}(t)\}) \tag{2.30}$$

Consequently, the mean value of $i(t)$ is

$$\overline{i(t)} = \overline{i_1(t)} - \overline{i_2(t)} = 2\mathcal{R}\sqrt{P_{LO}P_S}Re\{\underline{s}(t)\}\,. \tag{2.31}$$

On the other hand, the covariance function of the above current components are given by,

$$\begin{aligned} K_{i_1i_1}(t,u) &= q\overline{i_1(t)}\delta(t-u) \\ &\simeq q\mathcal{R}\frac{P_{LO}}{2}\delta(t-u)\,, \end{aligned} \tag{2.32}$$

$$\begin{aligned} K_{i_2i_2}(t,u) &= q\overline{i_2(t)}\delta(t-u) \\ &\simeq q\mathcal{R}\frac{P_{LO}}{2}\delta(t-u)\,, \end{aligned} \tag{2.33}$$

$$\begin{aligned} K_{ii}(t,u) &= K_{i_1i_1}(t,u) + K_{i_2i_2}(t,u) \\ &= q\mathcal{R}P_{LO}\delta(t-u)\,. \end{aligned} \tag{2.34}$$

The advantages of double detection configuration over single detection configuration is quite obvious. First, we get rid of the undesirable dc component simply by subtracting the currents. Second, any fluctuations in the local oscillator power is balanced by the corresponding increase or decrease in the two legs of the receiver yielding a more stabilized overall detection. Moreover, owing to the fact that the expression for the covariance function is the same for both the single and dual detector configurations, no extra penalty is paid.

2.5 Geometric Alignment Problems and Its Effect on Homodyning

So far in our calculations, we have assumed that the signal and LO fields are perfectly mode matched and geometrically aligned, i.e. they are incident upon the photodetector surfaces at the same points with the same beam waists and radii of curvature

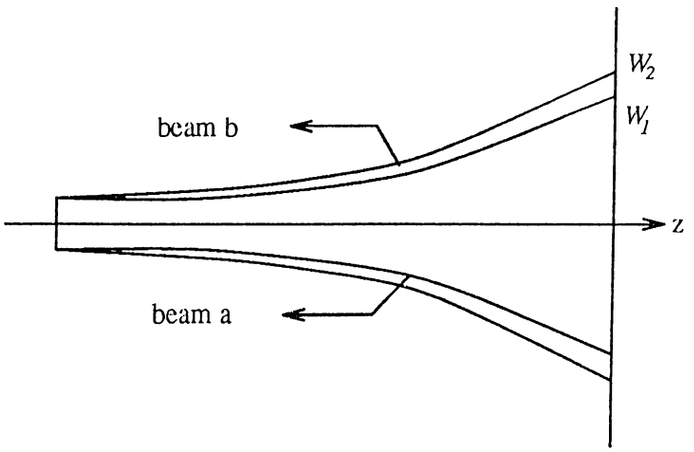

Figure 2.7: Misalignment of the LO and signal beam radii

after travelling identical paths. In reality, this is not so, and small deviations from ideal conditions are inevitable. In this section, types of alignment mismatches and their effect on the performance of the receiver is investigated. There can be two types of mismatch problems in an optical coherent receiver. They are,

i) *Radial Misalignment* : The beam radii of the signal and LO beams are not matched on the detector surface and,

ii) *Angular Misalignment* : The axes of propagation of the beams are not parallel and do not fall onto the detector surface perpendicularly.

In our treatment of these mismatches, we deal with them separately though calculation of these mismatches occuring together is fairly straightforward.

As was mentioned above, radial misalignment, relatively the simpler one of the two, occurs when both of the beams are perpendicularly incident on the photodetector surface with their axes of propagation perfectly overlapping each other but the beam radii on the photodetector surface plane are not of the same size. The beam radius $w(z)$ of a Gaussian beam is the point where the intensity of the beam falls to e^{-2} times its on-axis value[5]. The situation is depicted in figure 2.7. When beam a hits the photodetector surface, it has a beam radius of W_1 whereas beam b has a radius of W_2, where without loss of generality we assume that $W_2 > W_1$. Ideally, it would be best if the beams have the same radii and the photodetector surface is large enough to completely contain the spread of the beams. But beams with very

small radii are difficult to align and detectors with larger areas are generally slower in response[8]. The pin photodiodes used in the experiment have surface areas of 20 mm^2[13]. This, given the fact that the photosensitive areas are circular, corresponds to a radius of approximately 2.5mm, which, in turn, sets the practical limit on the radii of the beams. The normalized field associated with a radially symmetric Gaussian beam propagating along the z axis can be written as[10]

$$\overline{U}(r,z) = \left(\frac{2}{\pi}\right)^{1/2} \frac{e^{-j(kz-\phi(z))}}{w(z)} e^{-\left(r^2/w^2(z)+jkr^2/2R(z)\right)}, \tag{2.35}$$

where $w(z) = w_0\left(1+\lambda z/\pi w_0^2\right)^{1/2}$ is the beam radius, $R(z) = z\left(1+(\pi w_0^2/\lambda z)^2\right)$ is the radius of curvature and $\phi(z) = tan^{-1}(\lambda z/\pi w_0^2)$. Equation 2.35 implies that for two Gaussian beams $U_1(r,z)$ and $U_2(r,z)$ propagating along the z axis, the interference term would be

$$\begin{aligned} U_{INT} &= 2Re\{U_1(r,z)U_2(r,z)^*\}, \\ &= \frac{4}{\pi w_1(z)w_2(z)} e^{-r^2\left(\frac{1}{w_1^2(z)}+\frac{1}{w_2^2(z)}\right)}. \\ &\quad cos\left[\phi_1(z)-\phi_2(z)-kr^2\left(\frac{1}{R_1(z)}-\frac{1}{R_2(z)}\right)\right]. \end{aligned} \tag{2.36}$$

Integration of U_{INT} over the surface area of the photodetector yields the power generated by the interference term[3]. If this power is denoted by P_{INT} and the radius of photodetector surface by R, then

$$\begin{aligned} P_{INT} &= \frac{4}{\pi w_1(z)w_2(z)} \int_0^R d\overline{r}\, circ(\|\overline{r}\|/R) e^{-r^2\left(\frac{1}{w_1^2(z)}+\frac{1}{w_2^2(z)}\right)}. \\ &\quad cos\left[\phi_1(z)-\phi_2(z)-kr^2\left(\frac{1}{R_1(z)}-\frac{1}{R_2(z)}\right)\right]. \end{aligned} \tag{2.37}$$

The above integral is directly integrable and the final result as a function of the photodetector surface radius R is,

$$\begin{aligned} P_{INT} &= \frac{\frac{4}{w^2(z)}}{w_1(z)w_2(z)\left(\frac{1}{w^2(z)}+\frac{k^2}{R(z)^2}\right)}. \\ &\quad \left[cos\phi(z)+\frac{kw^2(z)}{R(z)}sin\phi(z)- \right. \\ &\quad \left. e^{-\frac{R^2}{w^2(z)}}\left(\frac{kw^2(z)}{R(z)^2}sin\left(\phi(z)-\frac{kR^2}{R(z)}\right)+cos\left(\phi(z)-\frac{kR^2}{R(z)}\right)\right)\right] \end{aligned} \tag{2.38}$$

where

$$\frac{1}{w^2(z)} = \frac{1}{w_1^2(z)} + \frac{1}{w_2^2(z)}, \tag{2.39}$$

$$\frac{1}{R(z)} = \frac{1}{R_1(z)} - \frac{1}{R_2(z)}, \tag{2.40}$$

$$and,\ \phi(z) = \phi_1(z) - \phi_2(z). \tag{2.41}$$

A plot of the above integral as a function of $\frac{w_2(z)}{w_1(z)}$ and R is provided in figure 2.8. In the plot, for any specific value of R, w_1 is always equal to $\frac{R}{2}$ and w_2 is varied from $\frac{w_1}{5}$ to w_1 in steps. Moreover, the interference power is normalized by the ideal interference power, i. e. the power we would obtain if w_1 were equal to w_2. As can be seen from the plot, for a specific ratio of the radii, the normalized power remains the same along the R axis. Other important things to note are : when the ratio of the beam radii is more than 0.64, the normalized power term is greater than 0.9 but

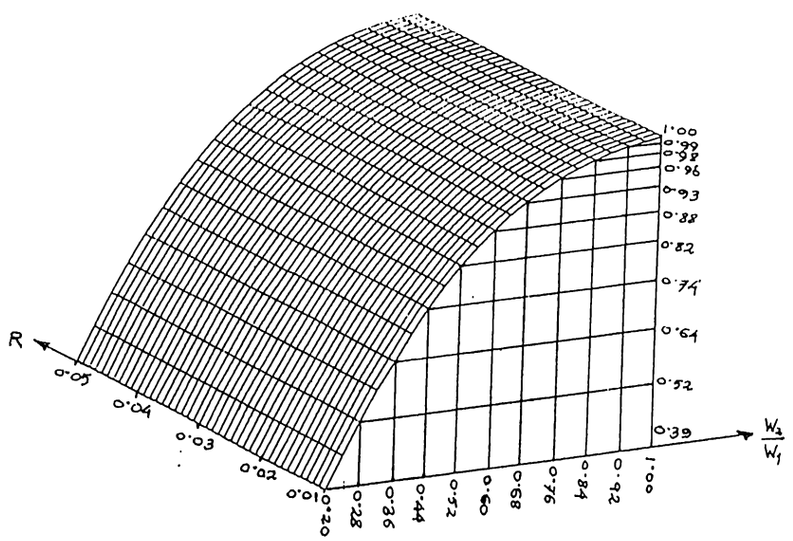

Figure 2.8: Normalized interference power plotted as a function of $\frac{w_2(z)}{w_1(z)}$ and R. For any value of R, w_1 is chosen to be $\frac{R}{2}$ and w_2 is varied from $\frac{w_1}{5}$ to w_1. The power is normalized by the ideal interference power,i.e. the power obtained when w_1 is equal to w_2.

the normalized power term falls below 60% of the ideal value when the ratio gets smaller than 0.36. The corresponding contour plot of the normalized interference power is also provided in figure 2.9. The gradual increase in the spacing between

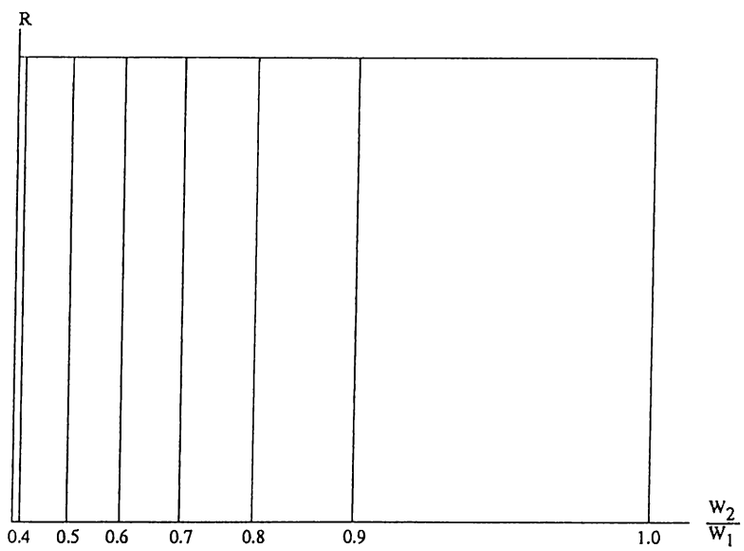

Figure 2.9: Contour plot of interference power plotted as a function of $\frac{w_2(z)}{w_1(z)}$ and R

contours of fixed difference should be noted.

It should be noted that the above calculations are carried out and plots drawn assuming that the signal and local oscillator fields are of equal power. In practice, the LO field is much powerful than the signal field and hence, it is always safer to keep the LO field radius slightly larger than the signal field radius to ensure that all of the weak signal field is interfered with the overwhelmingly strong LO field.

The other type of misalignment occurs when the beam radii of the beams match, but their axes of propagation do not. The situation is shown in figure 2.10. Both beams a and b are incident onto the photodetector surface. But, while beam a's axis of propagation is coincident with the z axis and hence perpendicular to the photodetector surface, beam b's axis of propagation makes an angle of θ with the z axis. As a consequence, though the radius of beam a is uniform and equal to $w(z_0)$ all over the photodetector surface [$z = z_0$ plane], the cross section of beam b at $z = z_0$ plane is a contour which is neither a circle nor an ellipse. Moreover, the beam radius of beam b is equal to $w(z_0)$ - the radius of beam a on the photodetector surface - only in one direction, along the y axis in the figure. This mismatch of the beams can again lead to power losses. To calculate the power loss precisely, let's look at the geometry involved with angular misalignment a bit more carefully. Let the direction

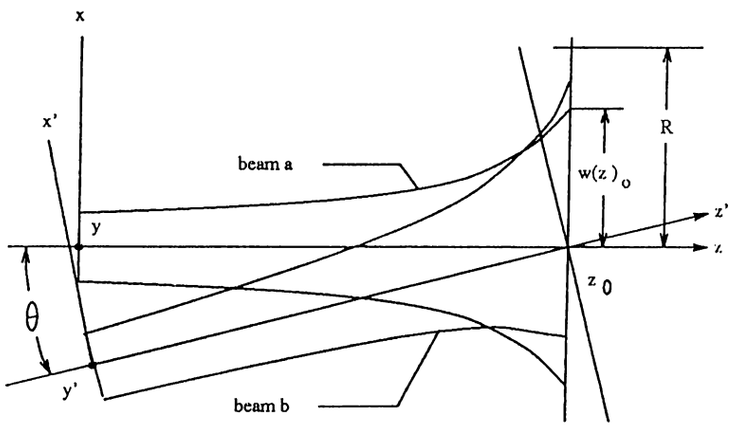

Figure 2.10: Misalignment of the LO and signal beam axes

of propagation of beam b be the z' axis (see figure 2.10). Then the detector surface intersects this axis at $z' = z_0$ and is located at the $x' = (cot\theta)(z' - z_0)$ plane. So, if beam b is represented by the field $U_2(x', y', z')$, its expression on detector surface plane would be

$$U_2(cot\theta(z' - z_0), y', z') = \sqrt{\frac{2}{\pi}} \frac{e^{-jkz' + j\phi(z')}}{w(z')} e^{-\left[cot^2\theta(z'-z_0)^2 + y^2\right]\left[1/w^2(z') + jk/2R(z')\right]} . \tag{2.42}$$

Now, using the transformations

$$x' = xcos\theta - zsin\theta + z_0 sin\theta , \tag{2.43}$$

$$y' = y , \tag{2.44}$$

$$and,\ z' = xsin\theta + zcos\theta + z_0(1 - cos\theta) \tag{2.45}$$

$U_2(cot\theta(z' - z_0), y', z')$ can be written as a function of x, y and z. With this rotated coordinate system representation, at $z = z_0$, $U_2(cot\theta(z' - z_0), y', z')$ equals $U_2(xcos\theta, y, z_0 + xsin\theta)$ which can be expressed as

$$U_2(x, y, z_0) = \sqrt{\frac{2}{\pi}} \frac{e^{-jk(z_0 + xsin\theta) + j\phi(z_0 + xsin\theta)}}{w(z_0 + xsin\theta)} \cdot e^{-\left[(xcos\theta)^2 + y^2\right]\left[1/w^2(z_0 + xsin\theta) + jk/2R(z_0 + xsin\theta)\right]} . \tag{2.46}$$

On the other hand, if beam a is represented by the field $U_1(x, y, z)$ propagating along the z axis, its expression on the detector surface plane would be

$$U_1(x, y, z_0) = \sqrt{\frac{2}{\pi}} \frac{e^{-j(kz_0 - \phi(z_0))}}{w(z_0)} e^{-\left[x^2 + y^2\right]\left[1/w(z_0)^2 + jk/2R(z_0)\right]} . \tag{2.47}$$

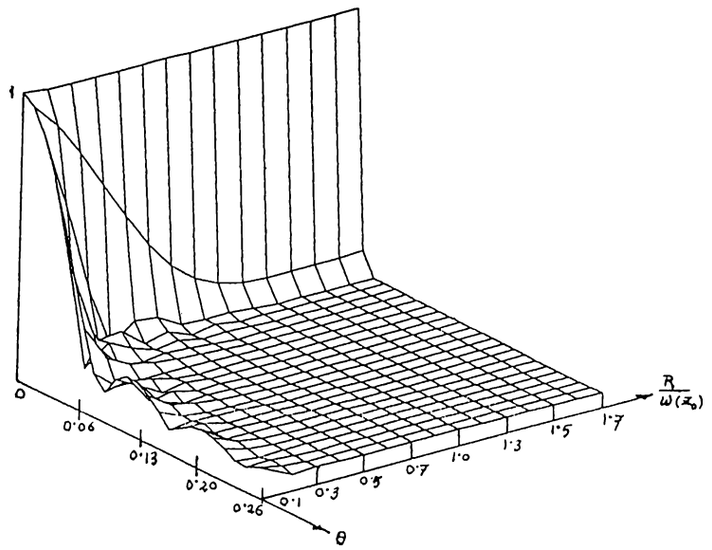

Figure 2.11: Normalized interference power plotted as a function of θ and $\frac{R}{w(z_0)}$. In the plot, $w(z_0)$ is fixed and the radius R is normalized by $w(z_0)$. At the same time, the power is also normalized by the ideal interference power, i.e. the power obtained for $\theta = 0$.

As a consequence, the interference term would now be

$$U_{INT} = \frac{2e^{-((xcos\theta)^2+y^2)/w^2(z_0+xsin\theta)-(x^2+y^2)/w^2(z_0)}}{\pi w(z_0)w(z_0+xsin\theta)} \cdot cos\left[\phi(z_0+xsin\theta)-\phi(z_0)-kxsin\theta-\frac{k((xcos\theta)^2+y^2)}{2R(z_0+xsin\theta)}+\frac{k(x^2+y^2)}{2R(z_0)}\right] \tag{2.48}$$

As was mentioned earlier integration of U_{INT} over the detector surface yields the interference power term. That is,

$$P_{INT} = \frac{2}{\pi w(z_0)}\int_0^R d\overline{r}\, circ(\|\overline{r}\|/R)\frac{e^{-((xcos\theta)^2+y^2)/w^2(z_0+xsin\theta)-(x^2+y^2)/w^2(z_0)}}{w(z_0+xsin\theta)} \cdot cos\left[\phi(z_0+xsin\theta)-\phi(z_0)-kxsin\theta-\frac{k((xcos\theta)^2+y^2)}{2R(z_0+xsin\theta)}+\frac{k(x^2+y^2)}{2R(z_0)}\right] \tag{2.49}$$

Unfortunately, the above integral is not analytically integrable and hence must be numerically computed. In figure 2.11, this term is plotted as a function of angular misalignment θ and normalized detector radius $\frac{R}{w(z_0)}$ for a fixed $w(z_0)$ [see figure 2.10]. Moreover, at each point, the value of the interference power is normalized

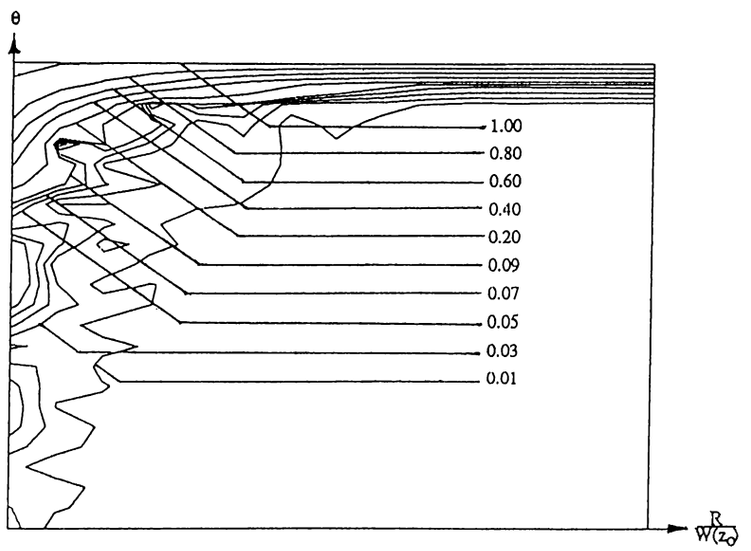

Figure 2.12: Contour plot of normalized interference power plotted as a function of θ and $\frac{R}{w(z_0)}$

by the ideal interference power (i.e. when $\theta = 0$) contained by the radius R. As can be seen from the plot, the interference power varies crucially as a function of misalignment angle θ and detector radius R. The general trends are that even for very small angles of misalignment, the interference power term vanishes to zero as the detector area gets arbitrarily large and that the tolerance of the interference power term to angular misalignment is particularly narrow. An angle of approximately 0.25° between the signal and LO beams is enough to reduce the power to negligible level. But what is interesting is, for a fixed angle, the interference power does not linearly go to zero as R increases. It passes through a few peaks and troughs as R increases before it eventually drops to zero. The reason behind this phenomenon will be explained in the next paragraph. For now, let's note that for a certain angle of misalignment, a detector with smaller surface area can do better than a detector with a larger surface area and will almost always outperform a detector with a very large area. But if the angle can be kept to zero or a value *very near to zero*, then a detector with a radius $R = w(z_0)$ will be adequate to contain most of the interference power. The contour plot of the normalized interference power term is shown in figure 2.12.

Experimentally, visual inspection, if possible, of the interference pattern of the local oscillator and the signal fields can be a very good indication of the precision of alignment achieved. In figure 2.13, enlarged photographs of interference patterns are shown. The interference pattern shown in figure 2.13.a refers to the case when the beams are misaligned by an angle of 0.1718°. In figure 2.13.b, where the misalignment is reduced to 0.0859°, the fringes get further apart. Finally, 2.13.c shows the interference pattern when the angle of misalignment is 0.0344°. As can

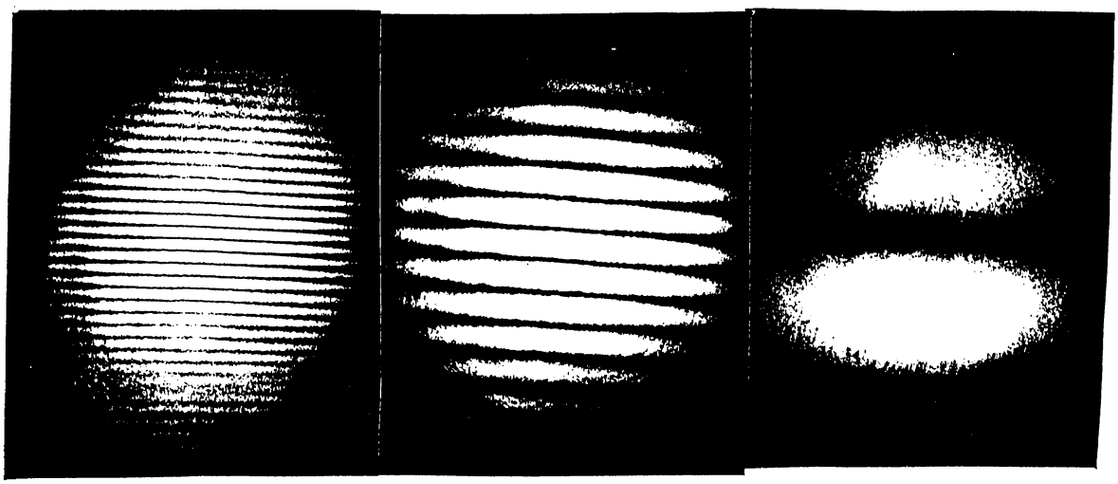

a) b) c)

Figure 2.13: Photographs of interference patterns for three different angles of misalignment: a) shows the interference pattern when the angle of misalignment between the LO and signal beams is 0.1718°, b) shows the interference pattern when the angle of misalignment between the LO and signal beams is 0.0859° and c) is for an angle of misalignment of 0.0344°.

be seen, the interference pattern consists of only a few fringes. Computer plots of interference patterns for the same angles is shown in figures 2.14, 2.15 and 2.16. The corresponding contour plots are shown in figures 2.17, 2.18 and 2.19. As can

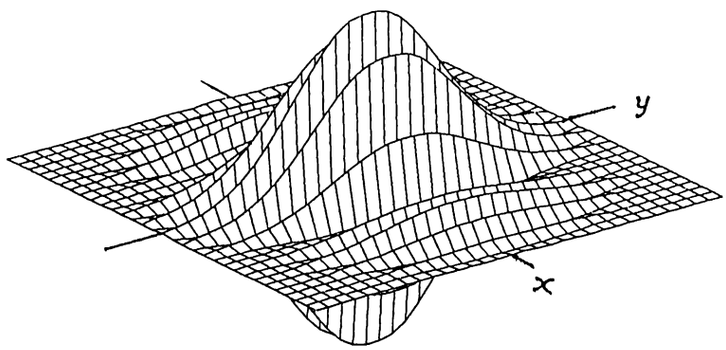

Figure 2.14: Computer plot of interference pattern for $\theta = 0.172°$

be seen from figures 2.14, 2.15 and 2.16, the suppressed sinusoid like lobes are symmetrical along the axis of misalignment [the x axis in figure 2.10] on the detector surface. Moreover, the number of lobes in the interference pattern increases as the angle of misalignment grows. These sinusoidal lobes are a direct consequence of the cosine term in the expression of U_{INT} in equation 2.48. The interference power term which is obtained by integrating the interference pattern over the detector surface averages these sinusoidal lobes. As a consequence, the worse the misalignment, the more wavy is the interference pattren, and hence, the lower the integrated power. Moreover, for a fixed angle of misalignment, as the detector radius R increases, the number of complete lobes contained by it changes and hence the power falls to zero in a suppressed sinusoid fashion. In any case, the photographs and computer plots comply with each other very closely. It should be mentioned that to clearly see the interference patterns, the LO power was attenuated to signal power levels.

It should be also noted that the penalty paid for axial misalignment is more if the fields are horizontally polarized than when they are vertically polarized. Let's suppose, for simplicity, that the LO field is a plane wave slightly offset from the

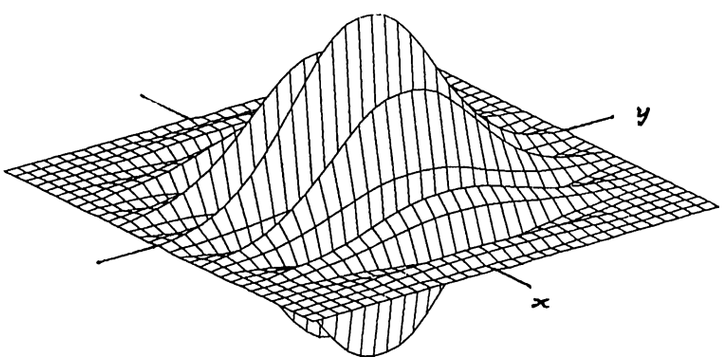

Figure 2.15: Computer plot of interference pattern for $\theta = 0.086°$

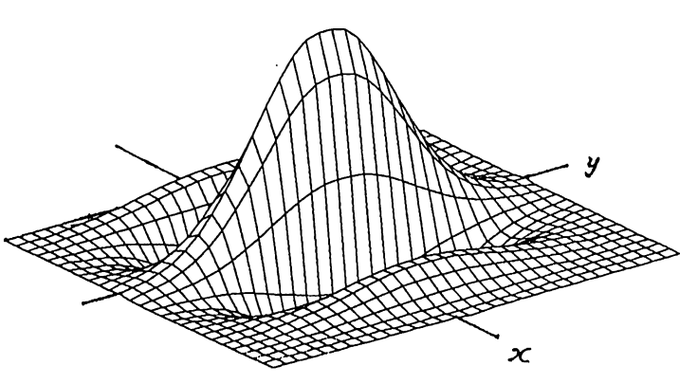

Figure 2.16: Computer plot of interference pattern for $\theta = 0.035°$

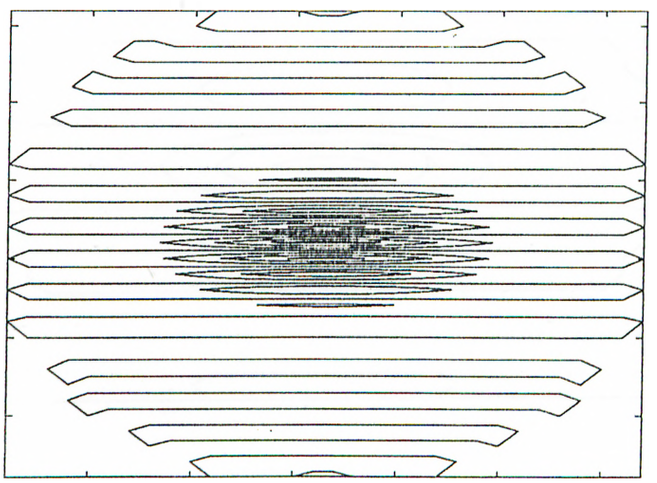

Figure 2.17: Contour plot of interference pattern for $\theta = 0.172°$

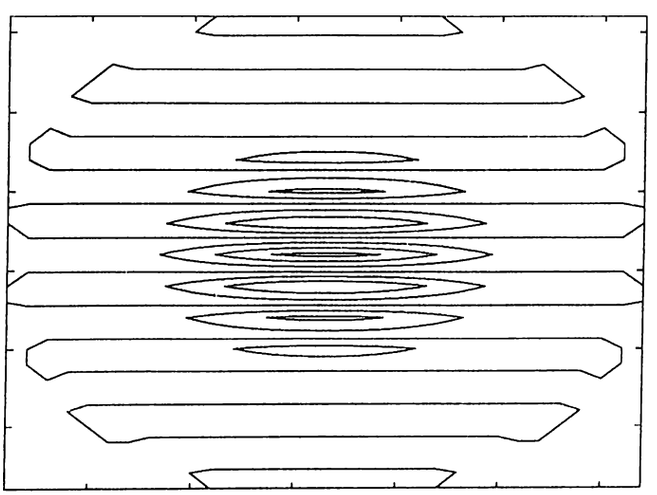

Figure 2.18: Contour plot of interference pattern for $\theta = 0.086°$

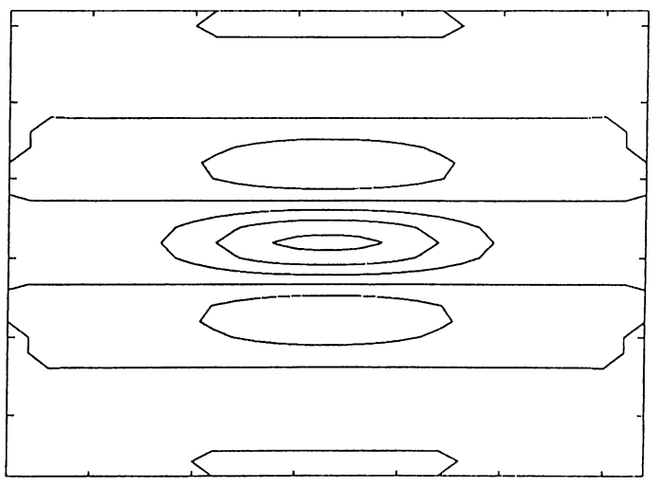

Figure 2.19: Contour plot of interference pattern for $\theta = 0.035°$

z axis towards the positive x axis by an angle of θ_x and is expressed as $\overline{U}_{LO}e^{j2\pi(fz+f_{x_0}x)-j(wt+\Phi_{LO})}$ where f_{x_0} is the x component of the spatial frequency $f = 1/\lambda$. The signal field, on the other hand, is slightly offset from the z axis towards the negative x axis by an identical angle of θ_x and, in turn, can be expressed as $\overline{U}_s e^{j2\pi(fz-f_{x_0}x)-j(wt+\Phi_s)}$. The orientation of the fields is shown in figure 2.20. The interference term which is of prime interest in homodyne detection is[11]

$$U_{INT} = 2\overline{U_{LO}} \bullet \overline{U_s} Re\{e^{j(4\pi f_{x_0}x+\Phi_{LO}-\Phi_s)}\}\,. \tag{2.50}$$

Now, if the field amplitude terms $\overline{U_{LO}}$ and $\overline{U_s}$ are vertically polarized, i.e. the direction of the corresponding electric field vectors are out of the page, then the interference term becomes

$$U_{INT} = 2U_{LO}U_s\cos(4\pi f_{x_0}x + \Phi_{LO} - \Phi_s)\,. \tag{2.51}$$

Whereas, for the field amplitude terms horizontally polarized, i.e. the electric field vectors lying on the plane of the page, we get an extra cosine term which diminishes the amplitude of the interference term,

$$U_{INT} = 2U_{LO}U_s\cos(2\theta_x)\cos(4\pi f_{x_0}x + \Phi_{LO} - \Phi_s)\,. \tag{2.52}$$

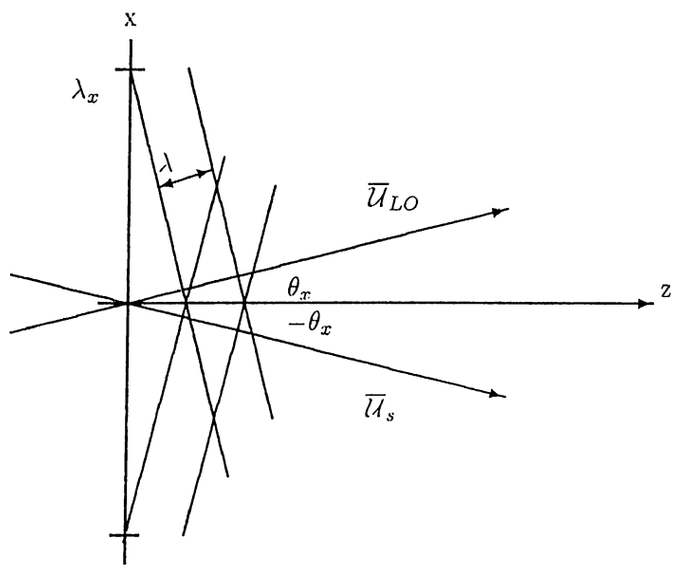

Figure 2.20: Simplified model of axial misalignment

So, we can conclude that for the same degree of axial misalignment, the horizontally polarized leg of the composite field coming out of the polarizing beam splitter PBS2 in figure 2.5 will suffer more loss than the vertically polarized leg.

Chapter 3

Results

3.1 Amount of Homodyning Obtained in the Lab

In section 2.4 we saw that the mean value of the total photodetector current in double detector configuration is $\overline{i(t)} = 2\mathcal{R}\sqrt{P_{LO}}Re(\underline{s}(t))$. This implies that if this current flows through a load resistance of $R\Omega$, and if binary Amplitude Shift Keying is employed to modulate the signal beam $P_s = P_H$ representing a logical high and $P_s = P_L$ representing a logical low, the voltage v_H across the load resistance corresponding to a logical high is

$$v_H = 2R\mathcal{R}\sqrt{P_{LO}P_H} \tag{3.1}$$

whereas, the voltage corresponding to a logical low is

$$v_L = 2R\mathcal{R}\sqrt{P_{LO}P_L}\,. \tag{3.2}$$

The photodetectors used in the experiment has the fastest response time with 50Ω load resistances. Their responsivities are approximately 0.427 A/W. This practically measured value of responsivity is somewhat higher than the value obtained from the responsivity curve provided in the data sheet (0.38 A/W). Consequently, with a local oscillator power of 2mW and P_H and P_L equal to 10μW and 0.5μW respectively,

$$\begin{aligned} v_H - v_L &= 2R\mathcal{R}\sqrt{P_{LO}}(\sqrt{P_H} - \sqrt{P_L}) \\ &= 2 \times 50\,\Omega \times 0.427A/W \times \sqrt{2mW}(\sqrt{10\mu W} - \sqrt{1\mu W}) \\ &= 5mV \end{aligned} \tag{3.3}$$

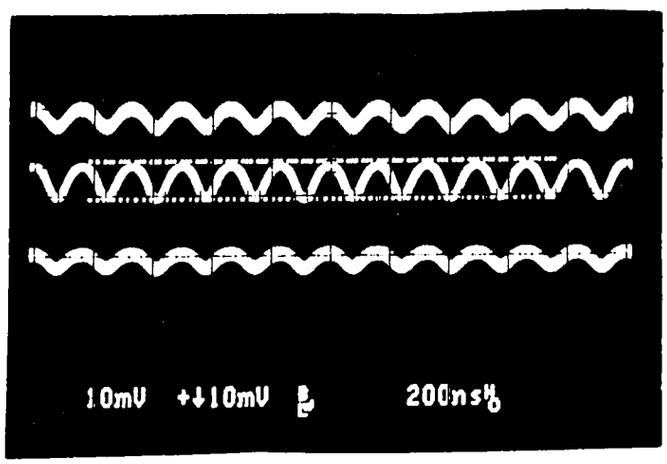

Figure 3.1: Homodyne detection of signal field

For the same local oscillator and signal powers employed in the lab, the value of $v_H - v_L$ obtained is very nearly equal to 5mV as shown figure 3.1. Figure 3.2 depicts the result of detecting the same signal in absence of the local oscillator field i.e. direct detection. As is visible from the figure 3.2, direct detection drastically fails to detect the signal field and hence, we see only noise on the oscilloscope. The signal detected in presence of the local oscillator field is shown in figure 3.1. The waveform in the middle corresponds to the double balanced detector output while the waveforms at the top and bottom correspond to the signals separately detected by the photodetectors. So, it can be safely concluded that the homodyning obtained in the lab very closely follows the theoretical calculations.

3.2 Noise Calculations

It is expedient to know the noise sources in the receiver and their types before getting into noise calculations. The expression for the autocovariance of the signal $x(t)$, which was derived in Chapter 1, consists of all the noise terms inherent and/or

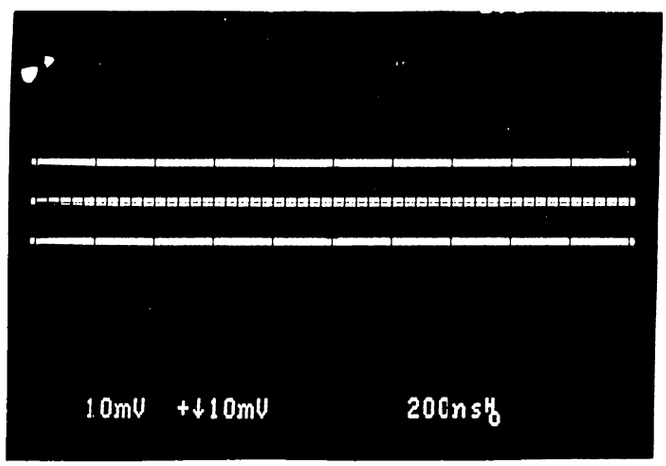

Figure 3.2: Detection of signal field in absence of local oscillator

added to the receiver. The expression is repeated below:

$$K_{xx}(t,u) = \left[q\mathcal{R}\left(P_{LO} + P_s\|\underline{s}(t)\|^2 + 2\sqrt{(P_{LO}P_s)}Re(\underline{s}(t))\right) + qI_D + 2kT/R\right] \quad (3.4)$$

where

$q\mathcal{R}P_{LO}$ is the shot noise caused by the local oscillator. It is directly proportional to the LO power and is usually the dominating noise term in coherent detection systems. For instance, for 10mW LO signal power, it will cause a noise level of $6.83 \times 10^{-22}A^2/Hz$ for the photodetectors used in our experiment.

$q\mathcal{R}P_s\|\underline{s}(t)\|^2$ is the shot noise caused by the signal. If the average signal power $P_S = P_s\|\underline{s}(t)\|^2$ equals 5μW, it will have a value of $3.42 \times 10^{-25}A^2/Hz$ which is negligible compared to the LO noise.

qI_D is the shot noise term caused by the dark current I_D of the photodetector. The photodetectors used in the experiment had average dark current values of $1.5 \times 10^{-7}A$. This corresponds to a noise level of $2.4 \times 10^{-26}A^2/Hz$ which is even more negligible compared to the LO noise term.

$2kT/R$ is the thermal noise current produced by the load resistance R. For a 50Ω load resistance this corresponds to a noise of $1.656 \times 10^{-22} A^2/Hz$. It should be noted that this is the only noise component comparable to the noise contributed by the LO .

The noise level shown by the HP network analyzer with its input short circuited is 120dBm/Hz with a resolution bandwidth of 100Hz. This noise level, when converted to the A^2/Hz unit above, corresponds to a noise level of $2 \times 10^{-19} A^2/Hz$. As can be seen, the noise of the analyzer is higher than the highest of the receiver noises by a magnitude of 10^3. Hence it was not possible to make precise measurements of the noise levels.

Chapter 4

Conclusion

The purpose of the thesis, as is explained in the introduction, was to gain hands-on experience in implementing optical homodyne detection receivers and related practical issues. As such this thesis will serve as a guideline for those who will work in the optics lab on experimental issues. As mentioned there, there is an acute lack of relevant information in the literature about down-to-earth practical problems involving optical set-ups. While constructing the experimental set-up of the self-homodyne detection, we came across practical problems whose solutions are not mentioned anywhere but which are of utmost importance for the proper functioning of the receiver. Hence, such an exercise in implementing a coherent detection set-up was both necessary and useful. For instance, one of the major practical problems faced in the laboratory was the misalignment of the signal and local oscillator beams incident onto the photodetector surface. It is seen that severe mixing losses can occur due to minute misalignments of the beams. To secure a homodyne mixing of no less than 50% of the ideal case, angular deviations of only a few tens of micro radians are tolerable.

The other major practical limitation was the relatively short coherence length of multimode lasers. But it is seen that if we design our system keeping the reduced temporal coherence of multimode lasers in mind, very satisfactory performance in terms of homodyne amplification can be obtained even at relatively low local oscillator power levels.

As a future topic of research, feasibility of receiver configurations employing

phase diversity techniques for multimode lasers can be investigated. As was explained in Chapter 2, the major drawback of the self homodyne setup was the short coherence length of multimode lasers which brought about the constraint that the signal and LO beams take paths differing from each other by no more than a distance of 5cm. By employing the technique known as phase diversity[7], the path difference between the beams can be varied arbitrarily with a penalty of less than 3 dbs. This means that transmission of signals through optical fiber could be incorporated for either or both of the beam paths. What is basically done in phase diversity is that one of the polarization components of the LO beam (it can be the signal beam as well) is phase shifted from the other by an angle of 90° at the receiver front-end. The advantage is that by using a detection configuration very similar to ours, the cosine component of the phase is detected by one photodetector while the sine component of the phase difference is detected by the other. Hence, even if there is no phase correlation between the signal and LO beams, the signal beam can be continuously detected by either of the two detectors in double detection configuration and appropriately processsed later[3].

Work also need to be done to find a more accurate model of multimode lasers taking into consideration the excess noise introduced in the system by the random power fluctuation among the modes. A more appropriate model of multimode lasers would directly translate to better receiver designs and more sensitive systems.

Appendix A

q-parameter Calculations for Gaussian Beams

Any Gaussian beam can be completely characterized by what is known as its q parameter[14]. The q parameter which is a complex composite of the beam radius w and radius of curavature R can be written as[10]

$$\frac{1}{q(z)} = \frac{1}{R(z)} - \frac{j\lambda}{\pi w(z)^2}. \tag{A.1}$$

The evolution of a Gaussian beam through free space or any lens system is determined by calculating the transformation of the q parameter after passing through the medium. If A, B, C, D are the elements of the ray matrix characterizing the medium, then the transformation can be described by

$$q_{out}(z) = \frac{Aq_{in}(z) + B}{Cq_{in}(z) + D} \tag{A.2}$$

where $q_{in}(z)$ and $q_{out}(z)$ are respectively, the input and output values of the q parameter. The beam waist w_0 and the radius of curvature R_0 at the output of the He-Ne laser used in the experiment is specified by the manufacturer as $1.25 \pm 0.1mm$ and ∞ respectively. Assuming that the exit apperture of the laser is situated at $z = 0$, the value of the q parameter at $z = 0$ is

$$\frac{1}{q(0)} = -\frac{j\lambda}{\pi w(0)^2}. \tag{A.3}$$

On the other hand, if we define the length between $z = 0$ and lens L1 as l_1 (see figure 2.5) and the the length between the lens L1 and photodetector surface PD1

as l_2, the ABCD matrix for this lens system can be expressed as

$$\begin{bmatrix} A & B \\ C & D \end{bmatrix} = \begin{bmatrix} 1 - \frac{l_2}{f} & l_1 - \frac{l_1 l_2}{f} + l_2 \\ -\frac{1}{f} & 1 - \frac{l_1}{f} \end{bmatrix} . \tag{A.4}$$

Here, f is the focal length of lens L1. For our setup,

$$\begin{aligned} w(0) &= 0.625mm \\ l_1 &= 62.5cm \\ l_2 &= 127.5cm \\ f &= 50cm \end{aligned}$$

Using equations A.2, A.3 and A.4 and the above values, we calculate $q(l_1 + l_2)$ to be equal to

$$q(l_1 + l_2) = 0.7721 + j\,0.1284 . \tag{A.5}$$

From the above value of $q(l_1 + l_2)$ and A.1

$$\begin{aligned} w(l_1 + l_2) &= 0.980\mu m \\ R(l_1 + l_2) &= 79.34cm \end{aligned}$$

As was mentioned in 2.3, the beam waist inside the acusto optic modulator should be the narrowest. To ensure that, the AOM is placed at the point where the signal beam is focused by lens L1. This point, after carrying out very similar calculations as above, turns out to be 52cm away from lens L1.

References

[1] Jeffery H. Shapiro. *Lecture Notes for Optical Detection & Communication* (M.I.T., 1982)

[2] Robert M. Gagliardi and S. Karp. *Optical Communications* (Robert E. Kreiger Publishing Company, Malabar, Florida, 1988)

[3] T. Okoshi and K. Kikuchi. *Coherent Optical Fiber Communications* (KTK Scientific Publishers/Tokyo, 1988).

[4] M. Young. *Optics and Lasers* (Springer-Verlag Berlin Heidelberg, 1986).

[5] A. E. Siegman. *Lasers* (University Science Books, Mill Valley, California, 1986)

[6] Andreas Papoulis. *Probability, Random Variables, And Stochastic Processes*(McGraw-Hill Book Company, 1984)

[7] T. G. Hodgkinson *et al*, "Demodulation of Optical DPSK Using In-Phase and Quadrature Detection," *Electronics Letters* Vol 21, No 19, 1985.

[8] H. Kressel (Editor), *Semiconductor Devices* (Springer-Verlag Berlin Heidelberg, 1980).

[9] Roger F. Harrington *Time-Harmonic Electromagnetic Fields* (McGraw-Hill, Inc, 1961)

[10] Amnon Yariv *Quantum Electronics* (John Wiley & Sons, 1989)

[11] E. Hecht *Optics* (Addison-Wesley Publishing Company,1987)

[12] Model N23080 Acousto Optic Modulator Operating Manual, Newport Electro Optics Systems, Inc. Melbourne, Florida 1987

[13] Type C30822 Photodiode Data Sheet, (RCA Electro Optics, Canada 1988)

[14] Emil Wolf and M. Born *Principles of Optics* (Pergamon Press, 1987)